Yapparova, A., Gabellone, T., Whitaker, F., Kulik, D. A., & Matthäi, S. K. (2017). Reactive transport modelling of hydrothermal dolomitisation using the CSMP++GEM coupled code: Effects of temperature and geological heterogeneity. *Chemical Geology*, *466*, 562-574. https://doi.org/10.1016/j.chemgeo.2017.07.005

Reactive transport modelling of hydrothermal dolomitisation using the CSMP++GEM coupled code: Effects of temperature and geological heterogeneity

Alina Yapparova[a,*], Tatyana Gabellone[b], Fiona Whitaker[b], Dmitrii A. Kulik[a], Stephan K. Matthäi[c]

[a] *Paul Scherrer Institute, Laboratory for Waste Management, 5232 Villigen PSI, Switzerland*
[b] *University of Bristol, School of Earth Sciences, Wills Memorial Building, Queen's Road, Bristol, BS8 1RJ, UK*
[c] *University of Melbourne, School of Engineering, Melbourne, 3010, Australia*

Abstract

Reactive transport simulations using our CSMP++GEM coupled code were applied to study the major controls on replacement dolomitisation and the development of dolomite geobodies in a hydrothermal setting. A series of 2D simulations show how elevated temperature and reactive surface area increase the rate of dolomitisation, and result in a dolomite replacement front that is both sharper and inclined at a higher angle from vertical. This inclination, an effect of gravity segregation, is apparent in thick homogeneous units, but in layered systems the lithological contrast determines the shape of the dolomite front. The increase in permeability resulting from porosity generation upon replacement of calcite by dolomite has a major effect on accelerating the overall progress of dolomitisation. In contrast, the changes in fluid density due to chemical reactions and the pressure dependence of thermodynamic data have a minor influence under simulated conditions. Primary dolomite forms slowly after complete replacement of host calcite, leading to porosity decrease, and is only locally important around the source of the hydrothermal fluid.

For a simple layered system, our model results are in excellent agreement

* Corresponding author. Present address: ETH Zurich, Institute of Geochemistry and Petrology. E-mail address: alina.yapparova@gmail.com

with those obtained using TOUGHREACT code. They do, however, show the advantage of unstructured triangular over structured rectangular meshes for resolving complex curved/inclined front shapes. Such meshes also offer benefits in simulating fault-controlled hydrothermal dolomitisation.

Our simulations predict dolomite geobodies comparable in scale and morphology to natural examples documented at outcrops, and underline the importance of understanding the permeability structure within and around the fault zone.

Keywords:
reactive transport modelling, hydrothermal dolomitisation, Gibbs energy minimization, finite element – finite volume method, unstructured grids

---

1. Introduction

Reactive transport modelling (RTM), which couples fluid flow and geochemical reactions along flow paths, is an emerging numerical tool which can be used to identify and quantify major controls on water-rock interaction, and can help to improve predictions of diagenetic modification of reservoir quality (Steefel et al., 2005; Agar and Geiger, 2015). Reactive transport phenomena involve the synergistic interplay of simultaneous chemical reactions and fluid transport in geologically heterogeneous rocks, which is not possible to understand with the help of transport-only or chemical speciation-only models.

RTM has already been extensively applied to study the formation of dolomites in low-temperature shallow reflux systems (Jones and Xiao, 2005; Garcia-Fresca et al., 2009; Al-Helal et al., 2012; Xiao et al., 2013; Gabellone and Whitaker, 2016; Gabellone et al., 2016; Lu and Cantrell, 2016), as well as during burial diagenesis by fluids circulating due to geothermal convection (Wilson et al., 2001; Whitaker and Xiao, 2010) and sedimentary compaction (Consonni et al., 2010; Frazer et al., 2014).

By contrast to these diagenetic environments, there have only been a limited number of RTM studies of dolomitisation driven by circulation of hydrothermal fluids. Nonetheless, hydrothermal dolomites (HTD) are of considerable economic interest as they can form targets for hydrocarbon production (Davies and Smith, 2006), or occur in association with Mississippi Valley-type (MVT) ore bodies (Qing and Mountjoy, 1994; Davies and Smith, 2006).

Hydrothermal dolomites form by ingress into a fault zone of *Mg*-rich fluids with a temperature that is elevated (by 5-10°C) relative to the host limestone (Machel and Lonnee, 2002), and are usually structurally controlled. HTD bodies can have a patchy and localised distribution around sub-seismic scale faults (Machel, 2004; Wilson et al., 2007; Lopez-Horgue et al., 2010), but can also occur as stratabound bodies extending laterally for several tens of kilometres away from the faults proposed to have sourced the hydrothermal fluids (Davies and Smith, 2006; Corbella et al., 2014; Dewit et al., 2014). Important uncertainties remain as to the controls on the nature of hydrothermal alteration and the extent to which this process can form laterally extensive dolomites. Alteration can either increase or reduce porosity and permeability, and prediction of the spatial distribution of hydrothermal dolomites can be challenging.

RTM simulations by Corbella et al. (2014) explored major controlling parameters on the development of stratabound dolomite bodies associated with fault-controlled hydrothermal fluids in the Benicàssim area (Maestrat Basin, eastern Spain). They concluded that layers with differences in permeability of two orders of magnitude are needed in order to produce the observed kilometer long dolomite bodies within the more permeable packstone-grainstone beds. The employed fluid (five times concentrated seawater at 100 °C) is preferentially focused in these more permeable layers with lateral fluxes of several meters per year.

Consonni et al. (2016) simulated hydrothermal dolomitisation occurring in a lacustrine limestone reservoir of the Toca Formation (West Africa) and identified permeability as the major control on the distribution of dolomitised bodies. These authors also recognised the importance of flow rate, flow duration and fluid composition in determining the lateral extent of dolomitisation away from the faults. By doubling the flow rate or the simulation time the volume of the completely dolomitised limestone was almost doubled. Similar conclusions were reached by Jones et al. (2010) whose 2D and 3D simulations of HTD show preferential dolomitisation of the hanging wall of the fault blocks and a strong control on the dolomitisation pattern by fault and matrix permeability variations as well as by brine composition.

Fault-related hydrothermal diagenesis was simulated in generic sub-seismic scale RTMs (Xiao et al., 2013), with *Mg*-rich hydrothermal fluids flowing through a simple rectilinear fault over tens of thousands of years leading to large scale HTD formation and significant reservoir quality modification.

Although a few RTM studies of hydrothermal dolomitisation have been

reported, the effect of some numerical solution features on the resulting dolomite bodies has not been studied in detail. For example, Corbella et al. (2014) performed a sensitivity analysis on the influence of temperature on the rate of dolomitisation, but the RTM code RETRASO used in their study did not include the permeability update from changing porosity. Both CSMP++GEM (Yapparova et al., 2017) and TOUGHREACT (Xu et al., 2004) have this feature implemented. Other features of CSMP++GEM, such as the dependence of thermodynamic data on fluid pressure, and of fluid properties on chemistry, are also lacking in many other RTMs.

This study has the twofold aim of (i) better understanding the main controls on rates and patterns of hydrothermal fault-controlled dolomitisation, and (ii) exploring the applicability of different numerical solution procedures in reactive transport modelling.

A model with homogeneous rock properties and another with two layers of contrasting permeability were set up in CSMP++GEM in order to explore how RTM results are affected by the mesh type and refinement, and by the permeability feedback on the flow. In particular, we aimed to discriminate between "true" modelling results and artefacts due to the employed numerical procedure and/or modelling set up. The results of the homogeneous reference model in CSMP++GEM were compared with those from a similar model built in TOUGHREACT.

We then used CSMP++GEM to simulate HTD development in a layered and faulted limestone system, using different fault geometries (with vertical and inclined fault planes) to examine controls on specific aspects of the geometry of dolomite bodies. Specifically, we intended to address these questions:

1. What are the main controls on the width and the inclination of the dolomitisation fronts?
2. In HTD systems, what controls the development of stratabound vs massive dolomite bodies?
3. How does the geometry of the fluid-sourcing fault and the presence of a sealing layer influence the dolomitisation pattern?

The paper ends with a discussion comparing HTD bodies predicted by our reactive transport simulations with those from Corbella et al. (2014), and with natural examples from various outcrops.

2. Methods

2.1. Reactive transport model

The new CSMP++GEM reactive transport code (Yapparova et al., 2017) was applied to simulate hydrothermal dolomitisation in 2D. A subset of models also uses TOUGHREACT (Xu et al., 2004) in order to provide a comparison between the codes.

CSMP++ allows flow simulations with transient pressure including gravity effects. It contains a mass conservative transport scheme and an accurate equation of state for saline water (Driesner and Heinrich, 2007). Governing equations for fluid flow and solute transport are solved using the finite element – finite volume method (Geiger et al., 2004).

Chemical equilibrium calculations at different temperatures and pressures are performed by means of the GEMS3K standalone kernel (Kulik et al., 2013). The kinetic rate of mineral precipitation is incorporated into the equilibrium calculations via the additional metastability constraints on mineral amounts (for a detailed description see Thien et al., 2014; Yapparova et al., 2017).

Transport-chemistry coupling is performed following the Sequential Noniterative Approach (SNIA)(de Dieuleveult et al., 2009) and includes the feedback of the diagenetic change in porosity and permeability. Porosity is updated based on the current mineral volumes, permeability is updated from the porosity using Kozeny-Carman empirical relation (Yapparova et al., 2017):

$$k^{n+1} = k^n \frac{(1-\phi^n)^2(\phi^{n+1})^3}{(1-\phi^{n+1})^2(\phi^n)^3}, \tag{1}$$

where k^{n+1} and ϕ^{n+1} are the permeability and the porosity at the next time step, respectively, and k^n and ϕ^n at the current time step.

The rate of calcite dissolution is orders of magnitude higher than the rate of dolomite precipitation, and thus in our simulations dolomite was a kinetically controlled mineral, and calcite was under thermodynamic control. The kinetic rate of dolomite dissolution/precipitation (in mol/s) was taken from Arvidson and Mackenzie (1999):

$$r = \kappa A(1-\Omega)^\eta, \tag{2}$$

where Ω is the ratio between the ion activity product and the solubility product ($log\,\Omega = \mathrm{SI}$, mineral saturation index), $\eta = 2.26$ is the reaction order,

Table 1: Thermodynamic data comparison: equilibrium constants at 1 bar, 25 °C

logK	PSI/Nagra	THERMODDEM
calcite	1.8490	1.8470
dolomite	3.5680	3.5328

A is the effective reactive surface area and κ is the temperature dependent rate constant.

A thermodynamic database suitable for both CSMP++GEM and TOUGHREACT was not available, and therefore we used two different databases containing quite close equilibrium constants. Table 1 presents logKs for calcite and dolomite that correspond to the following reactions:

$$CaCO_3 = Ca^{2+} + HCO3^- - H^+,$$
$$CaMg(CO_3)_2 = Ca^{2+} + Mg^{2+} + 2HCO3^- - 2H^+.$$

The PSI/Nagra thermodynamic database (Thoenen et al. 2014) was used to prepare the CSMP++GEM input in GEM-Selektor and in the simulation runs, while the THERMODDEM database (Blanc et al. 2012) was used in the TOUGHREACT simulations. The molar volume of calcite is $36.93\,cm^3/mol$ in both databases, and the dolomite molar volume is $64.34\,cm^3/mol$ in PSI/Nagra and $64.36\,cm^3/mol$ in THERMODDEM.

The extended Debye-Huckel activity model with parameters $b_\gamma = 0.064$ and $a_0 = 3.72$, derived by Helgeson et al. (1981), was used in both software packages.

2.2. Model geometries and computational grids

Three different model geometries were used in the simulations and for each model geometry several meshes were created. Different types of meshes used include: autoblock (structured rectangular mesh, where each rectangle has been divided into two equal triangles); patch dependent (an unstructured mesh with its elements forming a pattern); patch independent (an unstructured mesh with elements not following a particular pattern).

Firstly, for a 2D single layer rectangular $1000\,m$-long and $200\,m$-high model four different meshes have been created (see fig. 1): an unstructured patch independent coarse mesh with 1228 triangular elements and 675 nodes (average element area $163\,m^2$); an unstructured patch independent fine mesh

with 2674 triangular elements and 1398 nodes (average $75\,m^2$); an unstructured patch dependent mesh with 1214 triangular elements and 669 nodes (average $165\,m^2$); a structured mesh with 1166 right-angled triangles and 648 nodes (average $171\,m^2$). For comparison a homogeneous model was also developed in TOUGHREACT, with three uniform grids of 20, 10 and $5\,m$ size (500, 2000 and 8000 cells with areas of 400, 100 and 25 m^2, respectively).

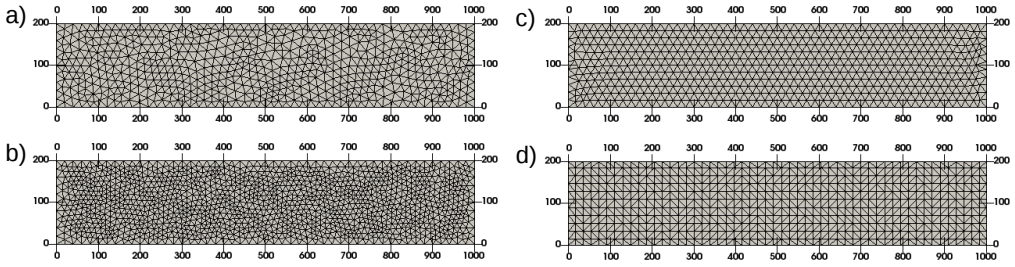

Figure 1: (a) unstructured coarse mesh, (b) unstructured fine mesh, (c) patch dependent mesh, (d) structured mesh

Secondly, for a 2D rectangular $500\,m$-long and $100\,m$-high model with two layers each $50\,m$-thick two unstructured patch dependent meshes were created (see fig. 2): one with the uniform cell size (1711 triangles and 940 nodes with average cells of $117\,m^2$) and the other one with a refinement along the boundary between the two layers (2486 triangles and 1309 nodes with average cells of $80\,m^2$).

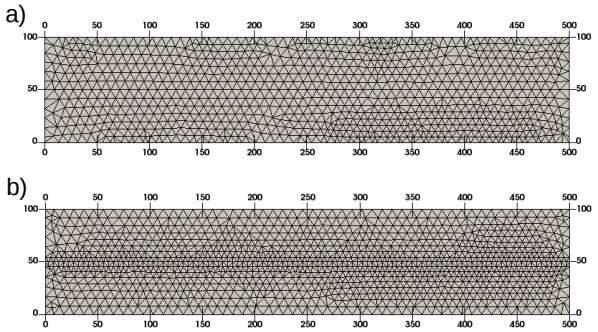

Figure 2: (a) uniform mesh and (b) mesh refined at the boundary between the high permeability and low permeability layers

Thirdly, a layered model geometry bisected by a fault extending from the top to the bottom of the grid was adapted from Corbella et al. (2014). It

is a 2D rectangular model, 1320 m long and 200 m high, with alternating 30 m and 40 m-thick layers, cross-cut by a 30 m wide vertical fault with the associated damage zone. A variant of this model is a 2D rectangular model with a normal fault, that dips at 60° and offsets the layers by 30 m.

Two different meshes were created for this setup; a patch dependent mesh for the model with a vertical fault (4614 triangular elements and 2446 nodes, average element area 77 m^2) and a patch independent mesh for the model with a normal fault (6250 triangles and 3289 nodes, average element area 32 m^2) (see fig. 3).

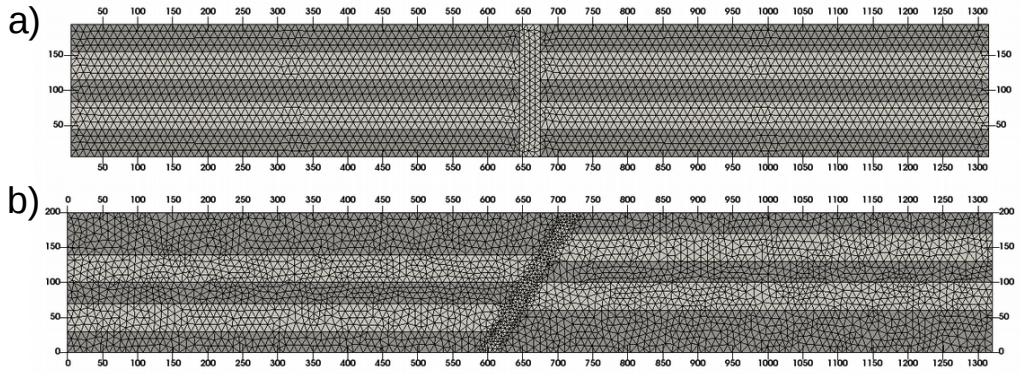

Figure 3: (a) mesh with a vertical fault and (b) mesh with a normal fault

All model geometries were created and meshed using ANSYS ICEM CFD.

2.3. Rock and fluid properties

Hydraulic properties of the rock based on petrographical observations for mudstone-wackestone, packstone-grainstone and the fault zone were adapted from Corbella et al. (2014). Porosity and permeability values are presented in Table 2.

Homogeneous models were populated with rock properties of a packstone-grainstone. In the two layer models a 50 m packstone-grainstone layer was underlain by a 50 m mudstone-wackestone layer. Initial porosity and permeability distribution of a double layer model is shown in Figure 4.

The layered models consist of two 30 m packstone-grainstone layers under- and overlain by 40 m mudstone-wackestone layers, and this sequence is cross-cut in the middle of the model by a 30 m wide fault with associated damage zone.

Table 2: Hydraulic properties of the rock. Fault zone properties are assumed to be independent of those of the matrix

Depositional/diagenetic texture	mudstone-wackestone	packstone-grainstone	damage zone fracturing
porosity, [-]	0.1	0.3	0.45
permeability, $[m^2]$	$1 \cdot 10^{-14}$	$3 \cdot 10^{-13}$	$5.8 \cdot 10^{-13}$

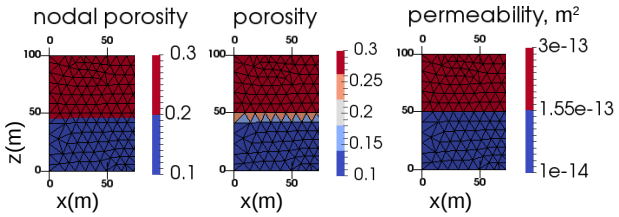

Figure 4: Initial nodal and elemental porosity and elemental permeability distribution for a two layer model

An initial mineral rock composition of 99% calcite and 1% dolomite was assumed. Three different values of effective specific reactive surface area for dolomite were used – 10 000 cm^2/g, 5000 cm^2/g, 1000 cm^2/g – which based on geometric calculations correspond to fine rhombs of 2.5 μm, 5 μm and 25 μm diameter, respectively.

The system was assumed isothermal and simulations were conducted at 70, 80, 90 and 100 °C and at the initial pressure of 110 bar (equivalent to the burial depth of 1120 m). Initial and injected (boundary) waters were derived from modern seawater (salinity 3.5%) from Nordstrom et al. (1979). For the initial water composition seawater was equilibrated with calcite and dolomite. To get the boundary water seawater was equilibrated with calcite only at pCO_2 values between 275 and 290 ppmv. The initial formation water plays little role as it is displaced by the injected boundary water within the first $100 - 200$ years of simulation. Table 3 summarizes the temperature dependence of the boundary solution composition at 100 bar in terms of total concentrations (molalities) of Independent Components (IC), pH, pe, pCO_2 (ppmv), Ionic strength (IS) (molal).

In addition, full chemical speciation of the boundary water at 100 °C is presented in Table 4.

Table 3: Boundary (injected) solution compositions at 70, 80, 90 and 100 °C, 110 *bar*

	70 °C	80 °C	90 °C	100 °C
SI dolomite	1.192	1.249	1.302	1.351
SI calcite	0	0	0	0
pH	7.418	7.388	7.368	7.343
pe	-4.211	-4.214	-4.234	-4.244
pCO_2	277	285	285	293
IS	0.679	0.677	0.676	0.674
C	$1.053 \cdot 10^{-3}$	$8.819 \cdot 10^{-4}$	$7.311 \cdot 10^{-4}$	$6.190 \cdot 10^{-4}$
Ca	$1.001 \cdot 10^{-2}$	$9.944 \cdot 10^{-3}$	$9.882 \cdot 10^{-3}$	$9.847 \cdot 10^{-3}$
Cl	$5.650 \cdot 10^{-1}$	$5.650 \cdot 10^{-1}$	$5.650 \cdot 10^{-1}$	$5.650 \cdot 10^{-1}$
H	$1.175 \cdot 10^{-3}$	$1.020 \cdot 10^{-3}$	$9.247 \cdot 10^{-4}$	$8.832 \cdot 10^{-4}$
K	$1.055 \cdot 10^{-2}$	$1.055 \cdot 10^{-2}$	$1.055 \cdot 10^{-2}$	$1.055 \cdot 10^{-2}$
Mg	$5.490 \cdot 10^{-2}$	$5.490 \cdot 10^{-2}$	$5.490 \cdot 10^{-2}$	$5.490 \cdot 10^{-2}$
Na	$4.839 \cdot 10^{-1}$	$4.839 \cdot 10^{-1}$	$4.839 \cdot 10^{-1}$	$4.839 \cdot 10^{-1}$
O	$1.196 \cdot 10^{-1}$	$1.192 \cdot 10^{-1}$	$1.187 \cdot 10^{-1}$	$1.184 \cdot 10^{-1}$
S	$2.917 \cdot 10^{-2}$	$2.917 \cdot 10^{-2}$	$2.917 \cdot 10^{-2}$	$2.917 \cdot 10^{-2}$
Si	$1.585 \cdot 10^{-4}$	$1.585 \cdot 10^{-4}$	$1.585 \cdot 10^{-4}$	$1.585 \cdot 10^{-4}$

Table 4: Boundary solution speciation at 100 °C

aqueous species	activity coefficient	molality concentration
$Ca(CO3)@$	1.1042456	5.58E-06
$Ca(HCO3)+$	0.6366374	1.32E-05
$Ca(SO4)@$	1.1042456	0.0007603803
$Ca+2$	0.12200329	0.0090649264
$CaOH+$	0.6366374	2.92E-06
$Ca(HSiO3)+$	0.6366374	1.59E-07
$CaSiO3@$	1.1042456	1.06E-08
$K(SO4)-$	0.6366374	0.0002584781
$K+$	0.6366374	0.010288142
$KOH@$	1.1042456	5.39E-08
$Mg(CO3)@$	1.1042456	9.02E-06
$Mg(HCO3)+$	0.6366374	6.91E-05
$Mg+2$	0.12200329	0.048933244
$MgOH+$	0.6366374	0.0001237188
$MgSO4@$	1.1042456	0.0057595896
$Mg(HSiO3)+$	0.6366374	1.17E-06
$MgSiO3@$	1.1042456	7.13E-07
$Na(CO3)-$	0.6366374	1.16E-06
$Na(HCO3)@$	1.1042456	6.69E-05
$Na(SO4)-$	0.6366374	0.0081254821
$Na+$	0.6366374	0.47567469
$NaOH@$	1.1042456	2.73E-06
$HSiO3-$	0.6366374	4.53E-06
$Si4O10-4$	0.0001645467	7.53E-19
$SiO2@$	1.1042456	0.0001518887
$SiO3-2$	0.12200329	2.31E-09
$CO2@$	1.1042456	2.55E-05
$CO3-2$	0.12200329	4.51E-06
$HCO3-$	0.6366374	0.0004241014
$CH4@$	1.1042456	1.33E-11
$ClO4-$	0.6366374	0
$Cl-$	0.6366374	0.56495312
$H2@$	1.1042456	1.07E-08
$N2@$	1.1042456	5.18E-06
$O2@$	1.1042456	0
$S2O3-2$	0.12200329	8.22E-10
$HSO3-$	0.6366374	1.84E-11
$SO3-2$	0.12200329	3.51E-11
$HSO4-$	0.6366374	1.16E-07
$SO4-2$	0.12200329	0.014119615
$H2S@$	1.1042456	1.01E-05
$HS-$	0.6366374	0.0001340185
$S-2$	0.12200329	1.64E-15
$OH-$	0.6366374	2.02E-05
$H+$	0.6366374	7.13E-08
$H2O@$	1.0015717	55.508373
mineral	log_{10}(SI)	
Graphite	-4.3446979	
Calcite	0.0001712937	
Ordered dolomite	1.3514311	
Anhydrite	-0.36738489	
Gypsum	-0.81832495	
Sulfur	-3.7878316	
Amorphous silica	-1.613096	

Table 5: Average values of fluid properties and pressure difference applied across the model at different temperatures

	70 °C	80 °C	90 °C	100 °C	Units
ρ	1006.2	1000.36	994.1	987.5	kg/m^3
μ	0.449	0.395	0.351	0.315	$mPa \cdot s$
Δp	3.3	2.9	2.55	2.3	bar

2.4. Initial and boundary conditions

An accurate calculation of the initial state is very important for reactive transport simulations. Initial model equilibration was performed in multiple steps. First, the pressure at the top model boundary was set to $110\,bar$ and the gravitational pressure distribution was calculated. Then, fluid properties were updated from the equation of state using the gravitational pressure field and specified constant temperature, and chemical equilibrium was calculated for every node at corresponding pressure-temperature condition. Additional boundary conditions were superimposed on the resulting pressure-temperature-chemical composition distribution. Specific boundary conditions for pressure were applied dependent on the flow scenario.

For the homogeneous and two layer models, Dirichlet boundary conditions for pressure were assigned on the left and right boundaries, hydrostatic on the right and super hydrostatic on the left, resulting in a uniform horizontal pressure gradient across the model. All homogeneous simulations started with an average lateral flow velocity of $2.2 \cdot 10^{-7}\,m/s$ ($6.94\,m/yr$, similar to the value of $6\,m/yr$ used in Corbella et al. (2014). Due to significant variations in fluid density and fluid viscosity at different temperatures distinct pressure difference values were used to achieve the desired flow velocity (see Table 5). A pressure difference of $2.3\,bar$ over $500\,m$ was used in the two layer simulations at 100 °C resulting in an average flow velocity of $4.6 \cdot 10^{-7}\,m/s$ in the high-k layer and $1 \cdot 10^{-8}\,m/s$ in the low-k layer. The left boundary consists of a non-reactive rock, amounts of calcite and dolomite were set to zero at the left model boundary and fixed through the entire simulation. The initial porosity and permeability values determined by the specified rock type were also fixed during the simulation.

For simulations with fluid flowing up the fault, the hydrostatic pressure distribution was held constant on the left and right model boundaries. A fixed overpressure boundary condition was applied at the bottom of the fault. Two

sets of simulations were performed: with a top boundary open for the outflow (constant pressure of 110 bar assigned), and with a closed top boundary. An overpressure of 2.9 bar (compared to the hydrostatic pressure value) at the bottom of the fault results in average flow velocities on the order of $10^{-6}\,m/s$ in the fault zone, $10^{-7}\,m/s$ in the high-k layers and $10^{-8}\,m/s$ in the low-k layers.

2.5. Time stepping

The Courant–Friedrichs–Lewy (CFL) condition is a necessary condition for convergence of a numerical solution of the transport equation. It is a time step restriction, that ensures that the fluid will move not more that one grid cell during a single time step. This is of particular importance for reactive transport simulations that use Sequential Non-Iterative Approach (SNIA). On one hand, the time step should be big enough for the fluid to react with the rock before it leaves the cell, on the other, if the time step of the transport-chemistry coupling is too small (much less than the one provided by CFL calculations) the fluid will react with the rock several times before leaving the cell and the amount of dissolved/precipitated minerals will be overestimated.

Simulations were carried out for time periods of tens of thousands of years with two nested time stepping loops. The pressure field was updated every 10 years and solute transport and chemical equilibrium/kinetic calculations were performed with a CFL restricted time step. Thus, for a homogeneous simulation CFL varied from $\sim$ 200 days in the beginning of the simulation to $\sim$ 50 days after complete dolomitisation.

3. Results

3.1. Comparison of CSMP++GEM and TOUGHREACT runs

Our reference simulation was conducted at 100 °C using all model features (porosity feedback, permeability feedback, salinity feedback, pressure dependence of chemistry) on a coarse unstructured grid (fig. 1a). The 1000 m-long and 200 m-high model was populated with the rock properties of a packstone-grainstone and dolomite RSA was set to 10 000 cm^2/g.

The results were compared to those obtained with TOUGHREACT on a grid with $20 \times 20\,m$ cell size (see fig. 5). A close match was achieved, with the position of the dolomite front in TOUGHREACT being very slightly ahead of

the one from CSMP++GEM. After 17 kyr of simulation time, 50 $vol\%$ of calcite is replaced by dolomite. Dolomite precipitation drives calcite dissolution, generating up to 9% additional porosity, and increasing permeability up to $8.6 \cdot 10^{-13}\, m^2$ (almost three times higher than the initial value of $3 \cdot 10^{-13}\, m^2$). The dolomite front is inclined, advancing more rapidly near the top of the model. Porosity reduction caused by primary dolomite cement precipitation after complete calcite replacement is prominent in the vertical zone over the first 50 m close to the injection point (left boundary). Horizontal flow velocity increases from the average value of $2.2 \cdot 10^{-7}\, m/s$ in the beginning of the simulation to an average of $3.4 \cdot 10^{-7}\, m/s$ after 17 kyr. Flow is almost exclusively horizontal, with a slight increase in horizontal velocity behind the dolomite front and a drop after it, and associated very minor changes in vertical flux.

Subsequently, we consider the relative time to fully dolomitise the reference case model (27.5kyr) to be equal to 1.

3.1.1. Mesh dependence

We compared simulations with different types of meshes: autoblock, patch dependent, patch independent mesh coarse and fine in CSMP++GEM and structured meshes with three different cell sizes in TOUGHREACT in terms of % dolomite after 25 kyr (fig. 6). These results highlight the advantage of unstructured over regular grids when simulating complex reactive transport phenomena. A fine unstructured grid accurately resolves the complex curved shape of the dolomitisation front. Coarse patch independent and patch dependent meshes provide similar results, showing a strong front inclination, whereas the autoblock mesh fails to capture the front shape, producing an almost vertical front. In addition, the front becomes sharper as the patch-independent grid resolution increases (as it is directly proportional to grid resolution). TOUGHREACT simulation results produce increasing numerical instabilities at the dolomite front with a decrease in cell size. We suggest the following explanation of this behaviour. With a finer grid, two small vertically neighbouring cells should have the same amount of dolomite, however, due to numerical instabilities the calculated amounts of dolomite diverge slightly. This difference is propagated to porosity and permeability and affects the flow field. In the subsequent time steps this small initial difference will be magnified, resulting in the development of channels of preferential flow and dolomitisation and resulting in the fingering of the dolomite front. In the simulation with a coarse grid, the front forms a “staircase” with no

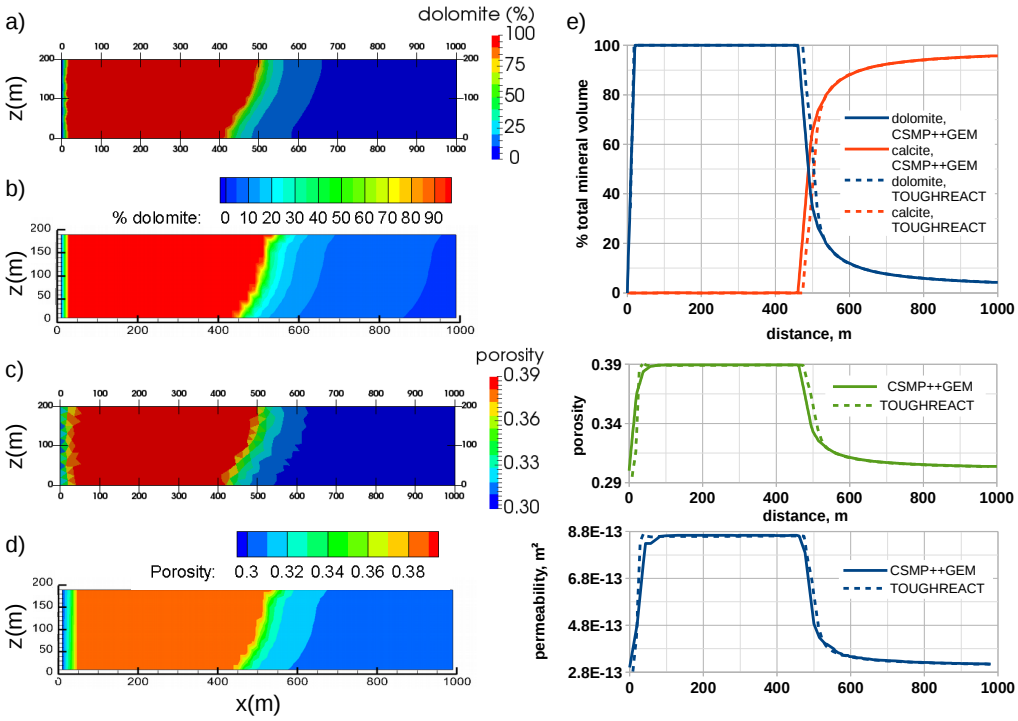

Figure 5: Results of the reference case simulation at 100 °C after 17 *kyr* (half of the model is dolomitised): dolomite, % total mineral volume (a) CSMP++GEM and (b) TOUGHREACT; porosity (c) CSMP++GEM and (d) TOUGHREACT; calcite is the reciprocal of dolomite, permeability distribution follows the porosity distribution; (e) compares changes in mineral amounts, porosity and permeability along the horizontal line through the middle of the model

two vertical neighbouring cells having the same amount of dolomite.

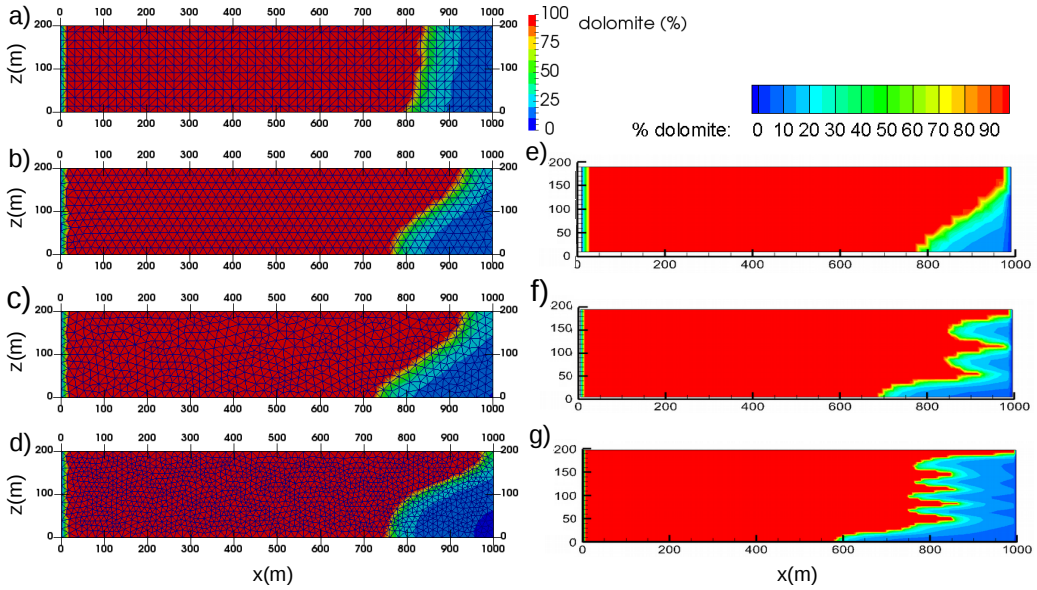

Figure 6: Dolomite, % total mineral volume, simulation results at 100 °C after 25 kyr: CSMP++GEM (a) autoblock mesh (b) patch dependent mesh (c) coarse patch independent mesh (10 m cell size) (d) fine patch independent mesh (5 m cell size); TOUGHREACT (e) 20 m square cells (f) 10 m square cells (g) 5 m square cells

3.2. CSMP++GEM features and their influence on modelling results

3.2.1. Permeability feedback

Mole per mole replacement of calcite by dolomite generates porosity due to the difference in molar volumes ($2 \times V_{calc}$ - $V_{dolo} = 2 \times 36.93 - 64.36 = 9.5$ cm^3/mol) and the resulting increase in calculated permeability facilitates the flow in the dolomitised zone. In order to assess this influence, we compared two simulations at 100 °C with RSA of 10 000 cm^2/g on the fine unstructured grid (fig. 1b) with and without permeability feedback on the flow (fig. 7a,b). When the permeability feedback is taken into account, 87.2% of the model is dolomitised after 25 kyr, compared with only 62.8% without the permeability feedback. Without this feedback the front is almost vertical with a minor deviation due to gravity segregation. The same behaviour is also observed in TOUGHREACT (fig. 7c).

Dolomitisation is a self-accelerating process that progressively develops a curved front shape over the long time. The initiation of a front that is slightly

inclined from the vertical is due to gravity segregation. In the upper part of the model fluid flows faster, replacing calcite with dolomite and increasing the permeability, which provides a positive feedback on the flow. Therefore over time the small initial instability develops into a complex front shape.

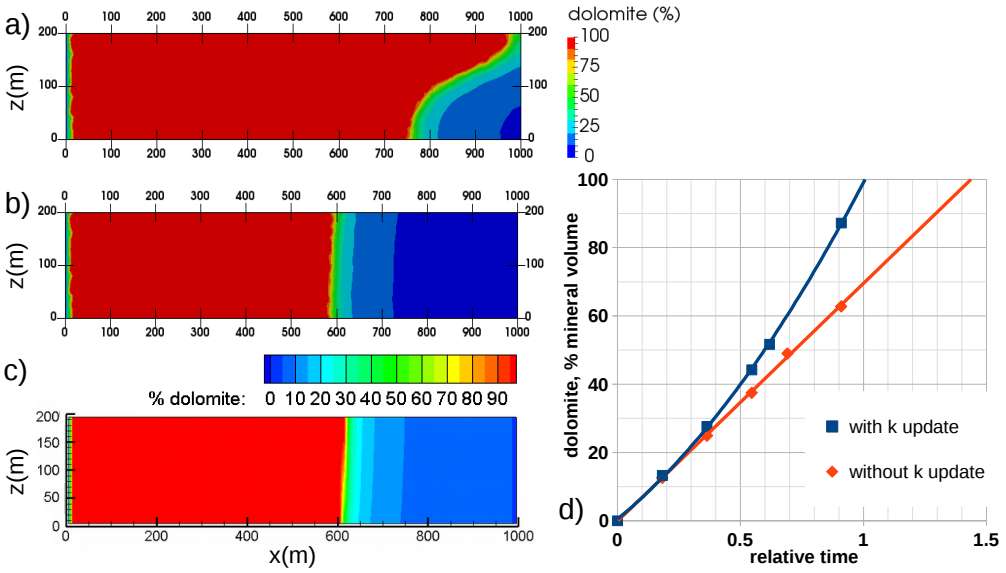

Figure 7: Dolomite, % total mineral volume, simulation results at 100 °C after 25 kyr (0.9 relative time): CSMP++GEM (a) with permeability feedback and (b) no permeability feedback; (c) TOUGHREACT without permeability feedback; (d) % dolomite versus relative time

Figure 7d highlights the non-linear nature of the dolomitisation process, provided by a positive permeability feedback on the flow. Without the permeability feedback it takes almost 1.4 times longer to completely dolomitise the model.

3.2.2. Salinity feedback

Equivalent salinity is calculated from the amount of dissolved solutes and is used to calculate the fluid properties (e.g. density and viscosity). Exchange of Mg^{2+} and Ca^{2+} ions during dolomitisation reduces fluid density behind the front. As a result of fluid gravity segregation, less dense fluids in the upper part of the bed move faster, thus accelerating dolomitisation. The resulting increase in porosity and permeability provides a positive feedback, increasing the difference between dolomitisation rates in the upper and the lower parts of the 2D domain.

Comparison of two simulations including and ignoring the mineral dissolution/precipitation feedback on the fluid properties via equivalent salinity (fig. 8) shows the difference in the density distribution behind and ahead of the dolomitisation front. In the simulation with a constant fluid salinity of 3.5% in the whole model, fluid density depends on the pressure only, as the temperature is assumed to be constant. The dolomitising front is steeper, with only slight retardation towards the base of the model. Nevertheless, mineral dissolution/precipitation feedback on the fluid salinity seems to have only a minor effect on the overall rate of dolomitisation, with an increase in fraction of dolomite after 25 kyr from 86.8% to 87.6% upon inclusion of the feedback.

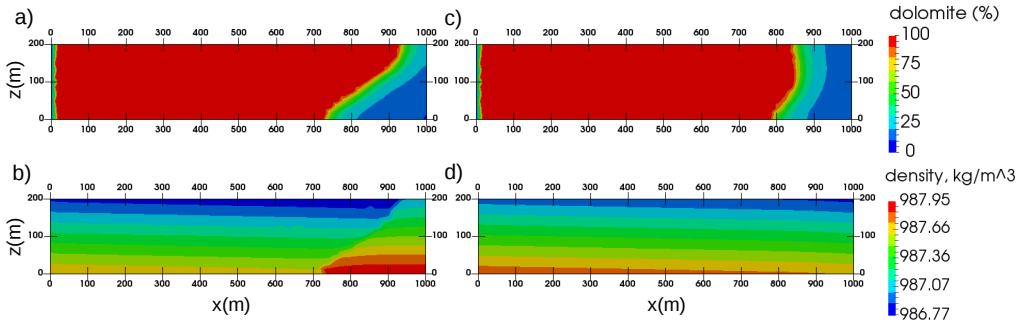

Figure 8: Simulation results at 100 °C after 25 kyr: dolomite, % total mineral volume and fluid density with salinity feedback (a,b) and no salinity feedback (c,d)

3.2.3. Pressure dependence of chemistry

In our simulations both pressure and temperature dependence of thermodynamic data were considered. However, simulations over the $110 - 130\,bar$ pressure range and equivalent depths at hydrostatic pressure suggest that pressure dependence has a negligible effect (results not shown).

3.3. Sensitivity studies

In this section we are looking at the main controls on the width and the inclination of the dolomitisation fronts.

3.3.1. Temperature influence on dolomitisation

Four simulations, at 70, 80, 90 and 100 °C were performed on the coarse mesh (fig. 1a) in order to assess the temperature influence on the dolomitising capacity of the seawater-derived fluid.

Temperature affects the dolomitisation rate both via thermodynamic controls (over the range of temperatures simulated dolomite saturation index (SI) increases with temperature) and kinetic controls (eq. 2). The time necessary to dolomitise the whole model at different temperatures (fig. 9e) becomes increasingly shorter as temperature increases. Compared to the 100 °C simulation, it takes 1.2 times longer to dolomitise the model at 90 °C, and 1.5 times and 2.2 times longer at 80 °C and 70 °C, respectively. Figure 9a-d compares the dolomite front in these simulations at the time when half of the model has been dolomitised. With an increase in temperature of the dolomitising fluid the transition zone between 100% dolomite and 100% calcite (the dolomitisation front) becomes narrower and orientated at an increasingly large angle from the vertical. After the complete replacement of calcite, dolomite continues to precipitate from the still oversaturated solution (termed overdolomitisation, *sensu* Lucia (2004)). For a $1000\,m$-long homogeneous model, overdolomitisation is observed in the first $80\,m$ adjacent to the left boundary, independent of temperature. The rate of dolomite precipitation was calculated from the decrease in porosity (fraction per $10\,kyr$) after porosity had reached its highest value. The porosity loss is the highest close to the inflow boundary and decays sharply over the first $50\,m$. (fig. 9f).

3.3.2. Sensitivity to reactive surface area

Using the coarse unstructured mesh (fig. 1a), we also evaluated the influence of changing RSA over an order of magnitude at 100 °C (fig. 10). The kinetic rate of dolomite precipitation increases with total RSA, which is controlled by both the specific RSA and the dolomite fraction. Comparing the fraction of model dolomitised versus relative time, increasing the RSA by an order of magnitude reduces the time to complete dolomitisation by a factor of 1.3. This is the cause of the non-linear increase in dolomitisation rate with fraction dolomitised that is apparent in all simulations. In addition, with an increase in RSA, for a given relative time the dolomite front becomes sharper and more inclined, reflecting the higher reaction rate. At lower RSA the curved shape of the dolomite front is developed at a later time.

3.3.3. Effects of contrasting layer permeability

We used the coarse double layer grid (fig. 2a) to compare two setups: a high-k layer underlain by a low-k layer and a high-k layer overlain by a low-k layer (fig. 11). The simulations at 100 °C assuming the RSA of $1000\,cm^2/g$ give symmetrically identical results; dolomitisation rate is an

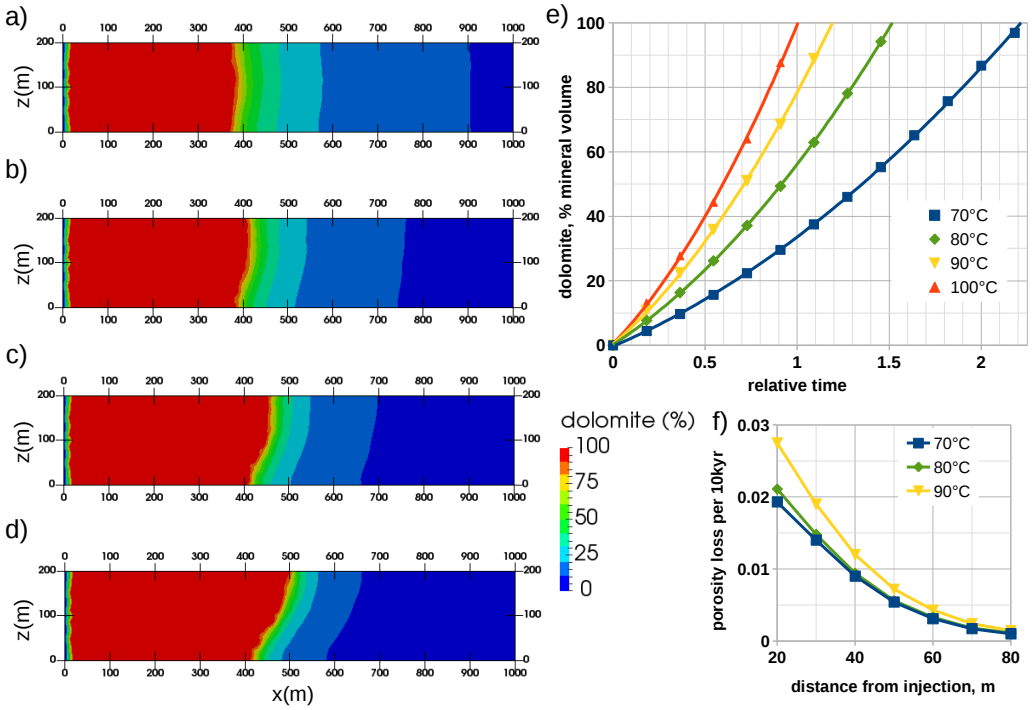

Figure 9: Dolomite, % total mineral volume, simulation results at different temperatures after half of the model has been dolomitised: (a) 70 °C after 37 kyr, (b) 80 °C after 25 kyr, (c) 90 °C after 20 kyr, (d) 100 °C after 17kyr; (e) dolomite, % total mineral volume versus relative time at different temperatures, (f) rate of dolomite cement precipitation (overdolomitisation) versus distance from injection (left boundary), after the model was completely dolomitised

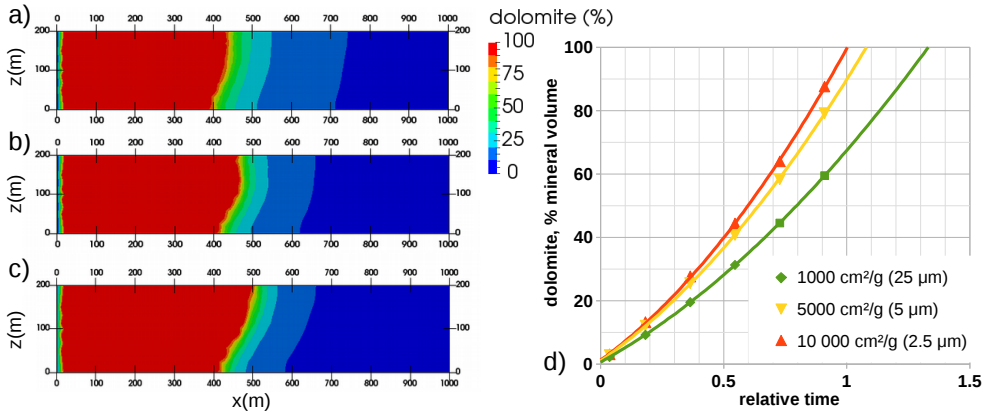

Figure 10: Dolomite, % total mineral volume, simulation results at 100 °C after half of the total calcite in the model was replaced: (a) RSA $1000\,cm^2/g$ after $22\,kyr$, (b) RSA $5000\,cm^2/g$ after $18\,kyr$, (c) RSA $10\,000\,cm^2/g$ after$17\,kyr$; (d) dolomite, % total mineral volume versus relative time for different RSA

order of magnitude higher in the high-k layer, in direct proportion to the higher flow velocity. The dolomite front in the low-k sediments is sharper and closer to vertical. Porosity at the time of complete calcite replacement increases to 39% from the initial 30% in the high-k layer and to 20% from the initial 10% in the low-k layer. This equates to the calculated increase in permeability from $3 \cdot 10^{-13}$ to $8.7 \cdot 10^{-13}\,m^2$ in the high-k layer and from $1 \cdot 10^{-14}$ to $8.0 \cdot 10^{-14}\,m^2$ in the low-k layer. Dolomite cement precipitation occludes the porosity and significantly reduces the permeability in the first $25\,m$ of the high-k layer.

In the homogeneous case an inclined front in the $200\,m$ layer was due to the gravity effects developing with time via permeability feedback. In contrast, in the simulations with two $50\,m$ layers the flatter gradient of the dolomite front within the high-k layer can be attributed to the influence of the underlying or overlying low-k layer. This behaviour can be explained by mixing between injected water supersaturated with dolomite from the high-k layer and the formation water in equilibrium of dolomite in the low-k layer. Within the part of the high-k unit that is adjacent to the low-k unit, this mixed fluid is less saturated to dolomite, and therefore less dolomite will precipitate at the boundary between the layers of contrasting permeability.

Two simulations with a uniform RSA $1000\,cm^2/g$ were performed on a uniform mesh and on a mesh refined at the boundary between the layers (see

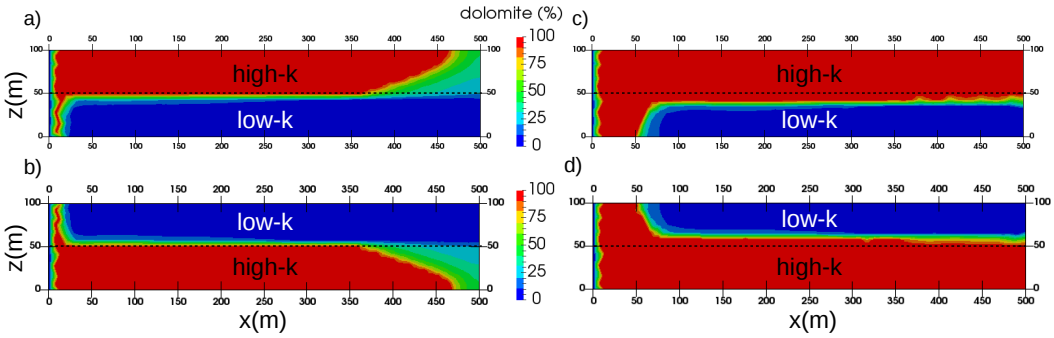

Figure 11: Dolomite, % total mineral volume in two layer models (a,b) after 12 *kyr* (1/2 of the model dolomitised) and (c,d) after 25 *kyr* (2/3 of the model volume was dolomitised). Calcite is the reciprocal of dolomite.

fig. 2 a,b) in order to find out if the mesh refinement has an influence on the width of the dolomitised fringe in the uppermost part of the low-k layer. The refined mesh can better resolve the transition between 100% dolomite and 100% calcite, but the width of the vertical penetration of the dolomite front into the low-k layer is the same (fig. 12). Figure 12c traces the vertical change in porosity through the middle of the model. It is clearly seen that the front is sharper with a finer mesh, but the quantitative difference in results is minor.

3.4. Modelling hydrothermal dolomitisation in a fault setting

A final set of models incorporated a permeable fault and associated damage zone which cuts a layered stratigraphy of alternating beds of high and low permeability limestone. These models all produce dolomite bodies with geometries comparable to those of hydrothermal dolomite bodies observed at several outcrops (Corbella et al., 2014; Sharp et al., 2010; Lopez-Horgue et al., 2010; Dewit et al., 2014). Four models are presented, which provide insight into the influence of fault geometry and permeability of fault zone and of boundary conditions on the patterns of hydrothermal dolomitisation.

3.4.1. Vertical fault

Figure 13 shows the simulation results after 30 *kyr* with fluids flowing up the vertical fault in the middle of the model and no offset of layers across the fault. Two boundary conditions were compared: an open top boundary (fig. 13a,b) and a closed top boundary (fig. 13c,d).

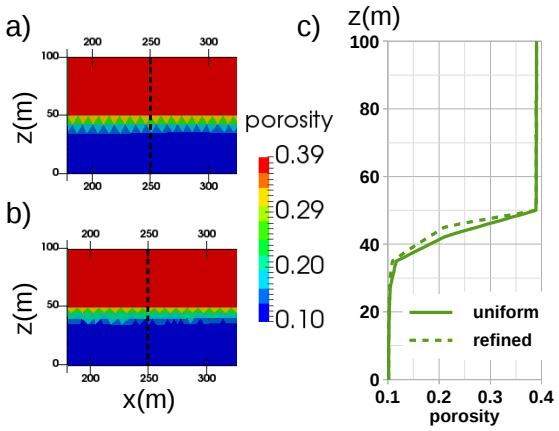

Figure 12: Porosity after 25 kyr of simulation at 100 °C: (a) uniform mesh, middle section of the model and (b) refined mesh; (c) plot over a vertical line at a distance of 250 m: uniform mesh and mesh refined at the boundary between the high-k and low-k layers; a sharper dolomite front is observed in the simulation with a refined mesh, but the width of the transition zone is equal for two simulations

In the case when fluids can escape through the top boundary, flow is largely constrained to the fault zone. Dolomite forms within the fracture zone with limited lateral extension into the adjacent matrix, at a rate which is largely independent of matrix permeability. Solute transport into the matrix adjacent to the fracture is largely by diffusion, explaining the limited width of the dolomite body and very sharp reaction fronts.

In the case of a closed top boundary, all fluids entering the model at the base of the fault discharge through the matrix. As a result, high-k layers are preferentially dolomitised, although the less permeable mudstone layers are also affected in the vicinity of the fault. The resulting dolomite body is laterally extensive; within individual layers the dolomite fronts are less sharp.

In both cases porosity increases by up to 7% in the fault zone, by 9% in high-k layers and to 10% in low-k layers from initial values of 45, 30 and 10% respectively, reflecting differences in the volume fraction of calcite available for dolomitisation. At the base of the fault porosity is reduced to 1-2% due to significant dolomite cement precipitation (overdolomitization), which has the effect of limiting the horizontal extent of dolomite in the lowest layer.

3.4.2. Normal fault

Figure 14 shows the simulation results for a model with a normal fault with and inclined plane and a vertical offset of layers of contrasting ma-

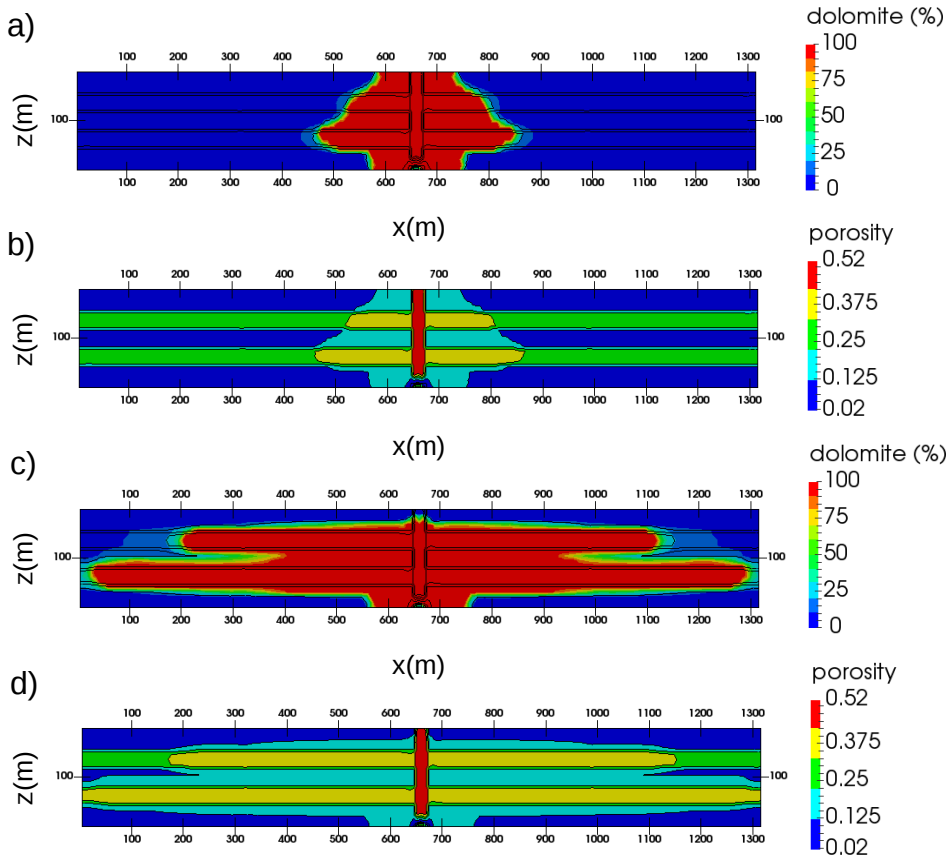

Figure 13: Simulation results at 100 °C after 30 kyr with fluids flowing up the vertical fault: (a, b) top boundary open for outflow; (c, d) closed top boundary. Black lines are porosity contours.

trix permeability. After 2.5 kyr (fig. 14a,d) a setup with an open top of the fault produces patterns where dolomite extends into high-k beds, although as dolomitisation proceeds intervening low-k beds are also dolomitised (fig. 14b,e).

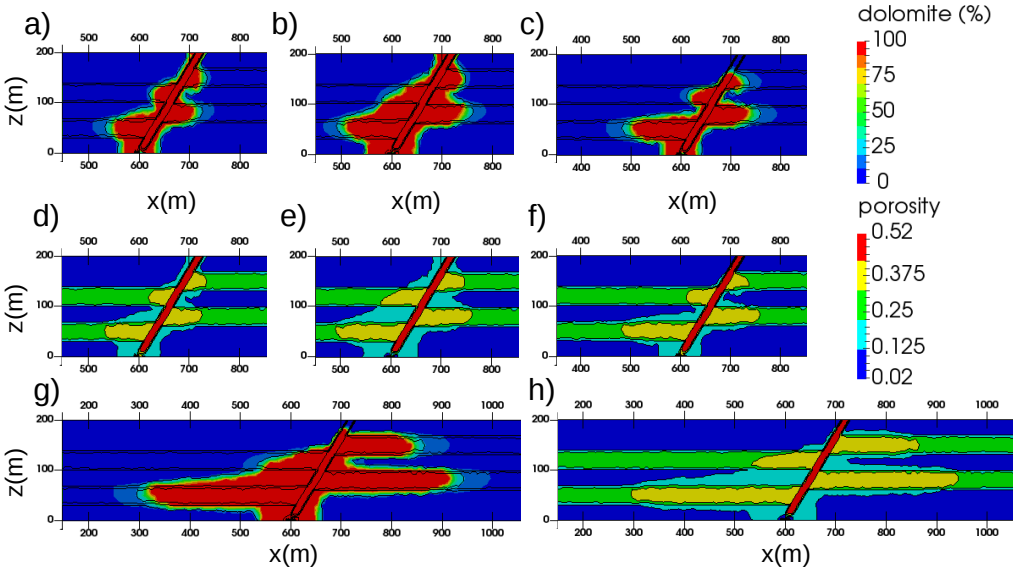

Figure 14: Dolomite, % total mineral volume and porosity, simulation results at 100 °C: open top boundary (a,d) after 2.5 kyr and (b,e) after 5 kyr; closed top boundary (c,f) after 5 kyr and (g,h) after 15 kyr. Porosity contours are shown in black lines.

Figure 14c,f-h shows the simulation results for a model with a normal fault sealed at the top boundary. This setup results in the preferential dolomitisation of high-k layers and produces stratabound dolomite bodies which extend laterally up to 300 m from the fault within 15 kyr. As also seen in the previous faulted models, the porosity reduction around the base of the fault limits dolomitisation extent of the lowermost layer. In both models with vertical offset, the dolomitisation front in the hanging wall shows less control by matrix properties. In contrast in the footwall matrix permeability affects the extent of lateral penetration of the dolomite front, which is 3 to 6 times greater in the high-k units than in the low-k units. All faulted models show a distinct reduction in the width of the dolomite body upon ascending along the fault towards the top of the model. However, within individual beds the slope of the dolomite front within high-k layers reflects contrasts in dolomitisation rate in underlying and overlying low-k beds.

4. Discussion

4.1. Effects of numerical solution procedure on modelling results

RTM simulations can provide an understanding of the operation of individual controls on complex coupled systems controlled by fluid flow, solute transport and water-rock reactions in a manner that is impossible to extract from natural systems. However, while in our simple homogeneous models we tried to decouple different model features, there always remains an interplay of various factors. For example, temperature of the dolomitising fluid plays a crucial role in controlling reaction rate, but its influence on buoyancy means that it is also strongly connected to the influence of gravity. In thin beds, gravity is less pronounced than in thicker beds. Both reaction rate and gravitational segregation affect the front shape. Our simulations illustrate why it is important to understand the fundamental processes governing behaviours of a simple modelled system before we can meaningfully apply the results of simulations to better understand natural systems.

The synergies between factors that influence the dolomitisation process are fundamentally dependent upon the feedback on the fluid flow from the permeability increase. This results in important non-linearities in the development of dolomitisation. However, the assumed relationship between modelled changes in porosity and the effective permeability is key.

An important application of simple homogeneous models is to understand the issues tied to the numerical solution procedure. The reactive transport system controlling even a simple replacement of calcite by dolomite is so complex that an analytical solution is not possible. Numerical solution is never exact and direct comparison of RTM simulations performed with different codes is challenging (Yapparova et al., 2017).

Our CSMP++GEM simulations generate consistent results and show that our code is applicable in practice. In contrast, our TOUGHREACT simulations with increasing mesh refinement show a diverging behaviour and increasing numerical instabilities.

Evaluation of the effect of differently structured meshes shows that we get quantitatively comparable results for different types of meshes, but there are small differences that are directly related to the mesh type. Structured corner-grid meshes are widely used in codes including TOUGHREACT (Xu et al., 2004) and our comparison here has shown that they cannot resolve some of the fine features.

Unstructured grids offer a number of important advantages, most importantly mesh refinement and adaptivity to non-linear geometrical features reflecting depositional facies, deformation features (i.e. faults, fractures) and prior diagenesis. Unstructured grids are already being used in the new generation reactive transport codes like PFLOTRAN (Lichtner et al., 2017).

A key challenge facing geologists with limited direct experience of process-based modelling is to understand which features of published simulations have broad applicability, and which originate from numerical procedures and model set-up. This can be exemplified by comparison between results from our double layer models and those of facies dependent dolomitisation in Early Cretaceous rocks at Benicàssim, Maestrat Basin, eastern Spain.

RTM simulations by Corbella et al. (2014) show preferential dolomitisation of the more porous and permeable packstone-grainstone layers, which over a long period of time also affects interbedded less porous and permeable mudstone-wackestone layers to produce massive dolomite bodies. Similar behaviour is observed in our models, although in simulations from Corbella et al. (2014) dolomitisation is much slower, despite using the same reaction kinetics. We attribute this difference to the incorporation in both our model and in TOUGHREACT of a feedback between evolving porosity and permeability, missing from the software used by Corbella et al. (2014). With this permeability update disabled, our models predict dolomitisation occurring more slowly and at a constant rate, independent of dolomite abundance. The increase in permeability during replacement phase makes dolomitisation a self-accelerating process: dolomitisation driving an increasing focus of reactive fluids in the more permeable beds and enhancing the permeability contrast between the beds. More rapid dolomitisation in the more permeable units also produces sharper dolomite fronts.

A further difference of some significance is that Corbella et al. (2014) assume that both calcite and dolomite are kinetically controlled minerals. As a result, in their simulations calcite dissolution and dolomite precipitation do not occur simultaneously: calcite is dissolved preferentially in the high-permeability beds whereas dolomite is mostly precipitated in the low-permeability beds (the opposite to that observed in the field). The apparent decoupling of the two reactions also does not accord with the chemical system that we model, which suggests that precipitation of dolomite is driving local calcite dissolution and that the dolomite growth rate is so slow that calcite effectively remains in local equilibrium with the fluid.

4.2. Fault-controlled dolomitisation and HTD geobodies

Our simulations of the faulted systems suggest that the style of dolomitisation is governed mainly by the presence or absence of a top seal. When a zone of low permeability prevents the vertical escape of diagenetic fluids flowing upward in a fault zone, the fringes of dolomite extend laterally into more permeable beds within the surrounding host rock. However, when the permeable fault conduit cross-cuts depositional stratigraphy and connects the reservoir of fluids to a sink (such as the sea floor), advection is largely constrained within the plane of the fault and the associated damage zone. Since, in this case, solute exchange with the rock matrix occurs largely by diffusion, dolomitisation only extends over short distances from the fault zone, forming a massive body with sharp diagenetic fronts.

Compared to the model with a displacive normal fault, a vertical fault without layer displacement produces a symmetrical dolomite body. Davies and Smith (2006) suggest a normal fault would result in a preferential dolomitisation of the hanging-wall site, due to the thermal gradient and fluids moving up due to gravity segregation. This accords with our models that show pervasive dolomitisation on the hanging-wall side and the development of stratabound dolomite bodies on the foot-wall side (fig. 14g).

The dolomitisation patterns presented in section 3.4 resemble those from a number of different outcrops, including the Zagros Mountains in Iran, the Canadian Rocky Mountains, and the Basque-Cantabrian Basin in the North of Spain, where dolomite geochemistry indicates formation from high temperature fluids (Sharp et al., 2010; Lopez-Horgue et al., 2010; Dewit et al., 2014). Although a detailed stratigraphic description of the dolomitised outcrops above Lake O'Hare in the Canadian Rocky Mountains (fig. 15) is not provided (Sharp et al., 2010), the majority of the dolomite fronts shows an upward sloping which supports our hypothesis of gravity segregation. The vertical development of these bodies is sometimes retarded or completely prevented by the presence of mudstone layers which acted as aquitards. Plume-like geometries develop immediately above the fault zone, whilst stratabound dolomite fingers form laterally away from the fault.

Two of our model setups (one with a top boundary open for the outflow and the other with a closed top boundary) can be considered as sections of a bigger scale model (fig. 15). Compared to the outcrops such as that in Iran and other field examples discussed by Sharp et al. (2010), the open boundary model corresponds to the lower section of the outcrop, close to the injection point and the closed boundary model corresponds to the section near the

sealing top layer. As observed in the field, close to the feeding point a bulbous dolomite body is formed within which dolomitisation is pervasive, although this does not extend far from the fault zone. Beneath a lower permeability layer, stratabound dolomite bodies are developed, within which the extent of dolomitisation is determined by differences in depositional texture. The patterns observed in our results also agree with generic patterns predicted by conceptual models of hydrothermal dolomitisation based on the distribution of fluid flux (Machel, 2004).

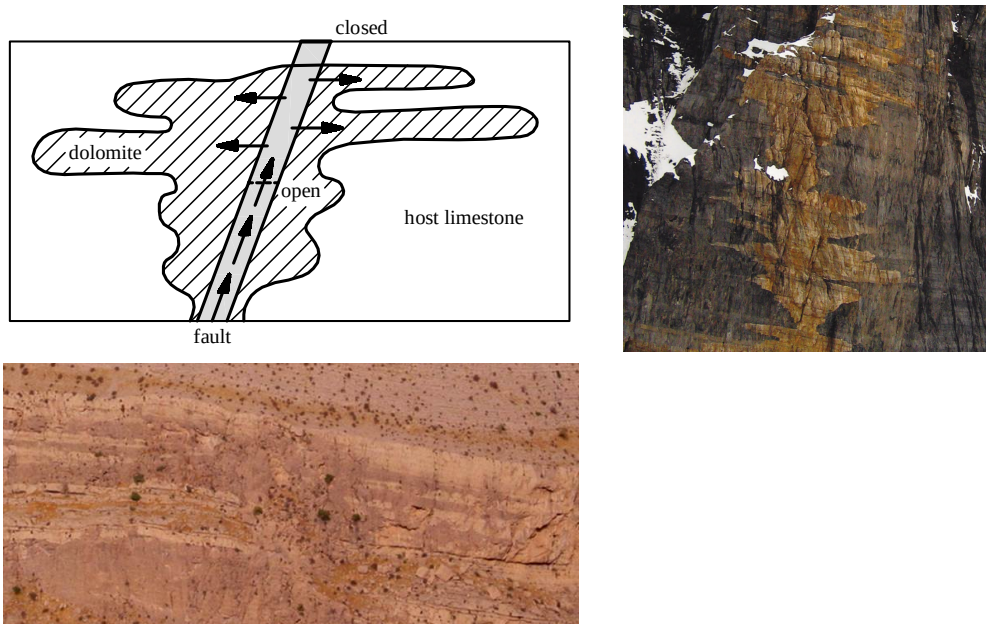

Figure 15: (top) Schematic representation of fault-controlled dolomitisation; (bottom) Outcrop photograph of a dolomite body, Zagros mountains, Iran, Sharp et al. (2010); (right) Outcrop photograph of a dolomite body, Canadian Rocky Mountains, Sharp et al. (2010)

Our modelling suggests that dolomitisation in fault-controlled systems can occur relatively rapidly, facilitated by high flow rates and temperatures that are thermodynamically and kinetically favourable. Within $2.5\,kyr$ the model setup with an open flow top boundary develops a "Christmas-tree" pattern (fig. 14a, compare to fig. 15). However, when the same setup is simulated over a more extended time, a massive dolomite body develops around the fault, with no indication of preferential dolomitisation of particular facies.

In nature, very sharp transition zones between dolomite and host lime-

stone are commonly observed at the boundaries of HTD bodies, frequently highlighted by colour change associated with iron-rich dolomitising fluids. However in some cases, e.g. in the Latemar (Jacquemyn et al., 2014), the colour change marks the contact between *Fe*-rich and *Fe*-poor dolomites rather than the limestone to dolomite transition. In nature, fronts may thus appear sharper than the underlying mineralogical transitions, and the latter are not always quantitatively evaluated.

Our models do predict sharp dolomitisation fronts within layered systems where flow and thus dolomitisation fronts are parallel to the bedding, as often observed in the field. Although less common, in some outcrops sharp fronts appear to have developed perpendicular to bedding. These are challenging to replicate in our models, although we can induce factors that favour this sharpening, including an increase in temperature and/or effective reactive surface area. An exception to this is in our models of faulted systems where flow is largely constrained to the fracture and associated damage zone, with limited exchange with the surrounding rock. Here the sharp fronts are again developed perpendicular to fluid flow, forming halos around fractures. Some previous RTM studies invoke a rather higher dolomite rate compared to that suggested by Arvidson and Mackenzie (1999) and used in most previous RTM simulations of dolomitisation (Jones and Xiao, 2005; Al-Helal et al., 2012; Gabellone et al., 2016). The use of a faster kinetic rate results in sharp dolomite fronts (Consonni et al., 2010).

Similarities between observed morphologies at a range of scales, from entire bodies to dolomite fronts, suggests our model captures processes that are important in natural systems.

5. Conclusions

Reactive transport simulations of hydrothermal dolomitisation (HTD) were performed using the new CSMP++GEM coupled code. The results presented here show the capabilities of the code and give an insight into the dolomitisation process and controls on the morphologies of HTD geobodies.

Comparing simulations using our code and TOUGHREACT showed results that are broadly in a good agreement, although they revealed certain problems with TOUGHREACT, including the lack of mesh convergence. CSMP++GEM results obtained with different mesh types highlight the superiority of a fine triangular mesh, although at computational cost. Two layer simulation results demonstrate that in a layered system there is no

need for mesh refinement along the boundary between the layers of different rock types.

Simple models with homogeneous rock properties allowed us to study the synergistic effect of gravity and permeability influence on the flow field in detail and to find a reasonable explanation for the self-accelerating nature of the dolomitisation process and the inclined shape of the dolomitisation front.

In a 200 m-thick homogeneous unit, gravity segregation initiates the front instability and via the permeability feedback promotes faster dolomitisation in the upper part of the model. However, with two 50 m thick beds of contrasting rock properties, the lower permeability bed has a crucial impact on the shape of the dolomitisation front in the higher permeability bed.

Although the feedback of chemical reactions on fluid salinity and the pressure dependence of thermodynamic data have a minor influence on the rate of dolomitisation progress and the shape of dolomitisation front, in a more complex scenario (concentrated seawater, higher pressure differences) these effects might play a more significant role.

With an increase in fluid temperature and reactive surface area the dolomitisation rate increases and the dolomite fronts become sharper (decreasing width of the transition zone from calcite to dolomite). Likewise, the rate of primary dolomite cement precipitation after complete calcite replacement increases with temperature.

Simulations of fault-controlled hydrothermal dolomitisation generate dolomite geobodies comparable in morphology to natural examples documented at outcrops, and underline the importance of permeability structure. In particular, our results show that stratabound dolomites tend to form in HTD systems when the fluids sourced from a fault encounter a low permeability barrier at the top of the fault. On the other hand, more massive dolomite bodies tend to form when the fault top is not sealed. The geometry of the fault has an effect on the dolomitisation trends, producing symmetrical bodies when it is vertical, or otherwise preferential alteration of the hanging-wall side when it is inclined and with layer displaced.

Our reactive transport simulations are currently limited to 2D due to the high computational cost, and thus may lack features which could emerge from simulation of HTD in 3D. There is ongoing development of the parallel version of CSMP++GEM that will increase the utility of our code and allow more complex reactive transport simulations.

Acknowledgements

We thank BG Group, Chevron, Petrobras, Saudi Aramco and Wintershall for sponsorship of the University of Bristol ITF (Industry Technology Facilitator) project IRT-MODE.

Authors are grateful to James Patterson for creating the ANSYS meshes. We appreciated productive discussions with Wilfred Pfingsten and Georg Kosakowski and their valuable insight into the TOUGHREACT comparison problem. Authors thank Zarema Amirova for drawing the fault-controlled dolomitisation sketch. We would like to thank the two anonymous reviewers for their comments that helped focus the paper and increase its readability.

Agar, S. M., Geiger, S., 2015. Fundamental controls on fluid flow in carbonates: current workflows to emerging technologies. Geological Society, London, Special Publications 406 (1), 1–59.

Al-Helal, A. B., Whitaker, F. F., Xiao, Y., 2012. Reactive transport modeling of brine reflux: dolomitisation, anhydrite precipitation and porosity evolution. Journal of Sedimentary Research 82, 196–215.

Arvidson, R., Mackenzie, F., 1999. The dolomite problem; control of precipitation kinetics by temperature and saturation state. Am. J. Sci. 299(4), 257–288.

Blanc, P., Lassin, A., Piantone, P., Azaroual, M., Jacquemet, N., Fabbri, A., Gaucher, E., 2012. Thermoddem: A geochemical database focused on low temperature water/rock interactions and waste materials. Appl. Geochem. 27(10), 2107–2116.

Consonni, A., Frixa, A., Maragliulo, C., 2016. Hydrothermal dolomitization: simulation by reaction transport modelling. Geological Society, London, Special Publications 435.

Consonni, A., Ronchi, P., Geloni, C., Battistelli, A., Grigo, D., Biagi, S., Gherardi, F., Gianelli, G., 2010. Application of numerical modelling to a case of compaction-driven dolomitization: A Jurassic palaeohigh in the Po Plain, Italy. Sedimentology 57 (1), 209–231.

Corbella, M., Gomez-Rivas, E., Martín-Martín, J. D., Stafford, S. L., Teixell, A., Griera, A., Travé, A., Cardellach, E., Salas, R., 2014. Insights to

controls on dolomitization by means of reactive transport models applied to the Benicàssim case study (Maestrat Basin, eastern Spain). Petroleum Geoscience 20 (1), 41–54.

Davies, G., Smith, L., 2006. Structurally controlled hydrothermal dolomite reservoir facies: An overview. AAPG Bull. 90(11), 1641–1690.

de Dieuleveult, C., Erhel, J., Kern, M., 2009. A global strategy for solving reactive transport equations. Journal of Computational Physics 228 (17), 6395–6410.

Dewit, J., Foubert, A., El Desouky, H. A., Muchez, P., Hunt, D., Vanhaecke, F., Swennen, R., 2014. Characteristics, genesis and parameters controlling the development of a large stratabound HTD body at Matienzo (Ramales Platform, Basque-Cantabrian Basin, northern Spain). Marine and Petroleum Geology 55, 6–25.

Driesner, T., Heinrich, C. A., 2007. The system H2O-NaCl . Part I : Correlation formulae for phase relations in temperature – pressure – composition space from 0 to 1000°C, 0 to 5000 bar, and 0 to 1 X_{NaCl}. Geochimica et Cosmochimica Acta 71, 4880–4901.

Frazer, M., Whitaker, F., Hollis, C., 2014. Fluid expulsion from overpressured basins: Implications for Pb-Zn mineralisation and dolomitisation of the East Midlands platform, northern England. Marine and Petroleum Geology 55, 68–86.

Gabellone, T., Whitaker, F., 2016. Secular variations in seawater chemistry controlling dolomitisation in shallow reflux systems: insights from reactive transport modelling. Sedimentology 63, 1233–1259.

Gabellone, T., Whitaker, F., Katz, D., Griffiths, G., Sonnenfeld, M., 2016. Controls on reflux dolomitisation of epeiric-scale ramps: Insights from reactive transport simulations of the Mississippian Madison Formation (Montana and Wyoming). Sedimentary Geology 345, 85–102.

Garcia-Fresca, B., Jones, G., Tianfu, X., 2009. The apparent stratigraphic concordance of reflux dolomite: new insights from synsedimentary reactive transport models. AAPG Convention, June 710, Search and Discovery Article N50208, Denver,Colorado.

Geiger, S., Roberts, S. G., Matthäi, S. K., Zoppou, C., Burri, A., 2004. Combining finite element and finite volume methods for efficient multiphase flow simulations in highly heterogeneous ans structurally complex geologic media. Geofluids 4, 284–299.

Helgeson, H. C., Kirkham, D. H., Flowers, D. C., 1981. Theoretical prediction of the thermodynamic behavior of aqueous electrolytes at high pressures and temperatures: Iv. calculation of activity coefficients, osmotic coefficients, and apparent molal and standard and relative partial molal properties to 600c and 5 kb. Am. J. Sci. 281, 1249–1516.

Jacquemyn, C., Desouky, H. E., Hunt, D., Casini, G., Swennen, R., 2014. Dolomitization of the latemar platform: Fluid flow and dolomite evolution. Marine and Petroleum Geology 55, 43–67.

Jones, G. D., Gupta, I., Sonnenthal, E., 2010. Reactive Transport Models of Structurally Controlled Hydrothermal Dolomite: Implications for Middle East Carbonate Reservoirs. In: 9th Middle East Geosciences Conference, GEO 2010. Vol. 16(2). GeoArabia, pp. 194–195.

Jones, G. D., Xiao, Y., 2005. Dolomitization, anhydrite cementation, and porosity evolution in a reflux system: Insights from reactive transport models. AAPG Bulletin 89 (5), 577–601.

Kulik, D. A., Wagner, T., Dmytrieva, S. V., Kosakowski, G., Hingerl, F. F., Chudnenko, K. V., Berner, U. R., 2013. GEM-Selektor geochemical modeling package: Revised algorithm and GEMS3K numerical kernel for coupled simulation codes. Computational Geosciences 17 (1), 1–24.

Lichtner, P. C., Hammond, G. E., Lu, C., Karra, S., Bisht, G., Andre, B., Mills, R. T., Kumar, J., Frederick, J. M., 2017. PFLOTRAN user manual. Tech. rep., http://www.documentation.pflotran.org.

Lopez-Horgue, M. A., Iriarte, E., Schroeder, S., Fernandez-Mendiola, P. A., Caline, B., Corneyllie, H., Fremont, J., Sudrie, M., Zerti, S., 2010. Structurally controlled hydrothermal dolomites in Albian carbonates of the Ason valley, Basque Cantabrian Basin, Northern Spain. Marine and Petroleum Geology 27 (5), 1069–1092.

Lu, P., Cantrell, D., 2016. Reactive transport modelling of reflux dolomitization in the Arab-D reservoir, Ghawar field, Saudi Arabia. Sedimentology 63, 865–892.

Lucia, J. F., 2004. Origin and petrophysics of dolostone pore space. In: Braithwaite, C., Rizzi, G., Darke, G. (Eds.), The geometry and petrogenesis of dolomite hydrocarbon reservoirs. Vol. 235. Geological Society (London) Special Publication, pp. 141–155.

Machel, H. G., 2004. Concepts and models of dolomitization, a critical reappraisal. In: Braithwaite, C., Rizzi, G., Darke, G. (Eds.), The geometry and petrogenesis of dolomite hydrocarbon reservoirs. Vol. 235. Geological Society (London) Special Publication, pp. 7–63.

Machel, H. G., Lonnee, J., 2002. Hydrothermal dolomite - A product of poor definition and imagination. In: 75th Anniversary of CSPG Convention, June 3-7, 2002. Canadian Society of Petroleum Geologists, pp. 1–8.

Nordstrom, D., Plummer, L., Wigley, T., Wolery, T., Ball, J., Jenne, E., Bassett, R., Crerar, D., Florence, T., Fritz, B., Hoffman, M., Holdren, G., Lafon, G., Mattigod, S., McDuff, R., Morel, F., Reddy, M., Sposito, G., Thrailkill, J., 1979. A comparison of computerized chemical models for equilibrium calculations in aqueous systems. In: Jenne, E. (Ed.), Chemical modeling in aqueous systems - Speciation, sorption, solubility, and kinetics. Vol. 93. American Chemical Society, Series, pp. 857–892.

Qing, H., Mountjoy, E. W., 1994. Formation of coarsely crystalline, hydrothermal dolomite reservoirs in the Presqu'ile barrier, Western Canada Sedimentary Basin. AAPG Bulletin 78 (1), 55–77.

Sharp, I., Gillespie, P., Morsalnezhad, D., Taberner, C., Karpuz, R., VergeS, J., Horbury, A., Pickard, N., Garland, J., Hunt, D., 2010. Stratigraphic architecture and fracture-controlled dolomitization of the Cretaceous Khami and Bangestan groups: an outcrop case study, Zagros Mountains, Iran. In: van Buchem, F. S. P., Gerdes, K., Esteban, M. (Eds.), Mesozoic and Cenozoic Carbonate Systems of the Mediterranean and the Middle East: Stratigraphic and Diagenetic Reference Models. Vol. 329. Geological Society, London, Special Publications, pp. 343–396.

Steefel, C. I., DePaolo, D. J., Lichtner, P. C., 2005. Reactive transport modeling: An essential tool and a new research approach for the earth sciences. Earth and Planetary Science Letters 240 (3–4), 539–558.

Thien, B., Kulik, D., Curti, E., 2014. A unified approach to model uptake kinetics of trace elements in complex aqueous-solid solution systems. Appl. Geochem. 41, 135–150.

Thoenen, T., Hummel, W., Berner, U., E., C., 2014. The psi/nagra chemical thermodynamic database 12/07. PSI Bericht 14-04, Paul Scherrer Institut, Villigen, Switzerland.

Whitaker, F. F., Xiao, Y., 2010. Reactive transport modeling of early burial dolomitization of carbonate platforms by geothermal convection. AAPG Bulletin 94 (6), 889–917.

Wilson, A. M., Sanford, W., Whitaker, F., Smart, P., 2001. Spatial patterns of diagenesis during geothermal circulation in carbonate platforms. Am. J. Sci. 301, 727–752.

Wilson, M. E. J., Evans, M. J., Oxtoby, N. H., Nas, D. S., Donnelly, T., Thirlwall, M., 2007. Reservoir quality, textural evolution, and origin of fault-associated dolomites. AAPG Bulletin 91 (9), 1247–1272.

Xiao, Y., Jones, G., Whitaker, F., Al-Helal, A., Stafford, S., Gomez-Rivas, E., Guidry, S., 2013. Fundamental approaches to dolomitisation and carbonate diagenesis in different hydrogeological systems and the impact on reservoir quality distribution. In: International Petroleum Technology Conference, Beijing, China. pp. 1164–1179.

Xu, T., Sonnenthal, E., Spycher, N., Pruess, K., 2004. TOUGHREACT user's guide: a simulation program for non-isothermal multiphase reactive geochemical transport in variable saturated geologic media. ReportLBNL-55460. Lawrence Berkeley National Laboratory, Berkeley, CA.

Yapparova, A., Gabellone, T., Whitaker, F., Kulik, D. A., Matthäi, S. K., 2017. Reactive transport modelling of dolomitisation using the new CSMP++GEM coupled code: governing equations, solution method and benchmarking results. Transport in Porous Media 117 (3), 385–413.